Towards understanding of the active sites for ORR in N-doped carbon materials through a fine-tuning of nitrogen functionalities: An experimental and computational approach.

Javier Quílez-Bermejo[1], Manuel Melle-Franco[2], Emilio San-Fabián[3], Emilia Morallón[3], Diego Cazorla-Amorós[1]

[1]Departamento de Química Inorgánica and Instituto de Materiales. Universidad de Alicante, Ap. 99, 03080, Alicante, Spain

[2]CICECO – Aveiro Institute of Materials, Department of Chemistry, University of Aveiro, 3810-193 Aveiro, Portugal

[3]Departamento de Química Física and Instituto de Materiales. Universidad de Alicante, Ap. 99, 03080, Alicante, Spain.

Abstract

The design of advanced N-doped carbon materials towards oxygen reduction reaction (ORR) catalysis is only possible if the nature of the active sites is fully understood. There is an important piece of research seeking to overcome this challenge through experimental or theoretical results. However, the combination of both approaches is necessary to deepen into the knowledge about this subject. This work presents excellent agreement between experimental results and computational models, which provides evidence about the nature of the most active sites in N-doped carbon materials. N-doped carbon materials have been experimentally obtained through double stage treatment of polyaniline in distinct atmospheres (both oxygen-containing and inert atmosphere) at different temperatures (800-1200ºC). According to temperature programmed desorption (TPD), Raman spectroscopy, N_2-adsorption isotherms at -196ºC and X-ray photoelectron spectroscopy (XPS), this synthesis method provides the selective formation of nitrogen species, without important changes in structural order or porosity. ORR catalytic tests evidence the highly efficient catalysis, with platinum-like performance in current density and onset potential, of N-doped carbon materials selectively containing graphitic-type nitrogen

species. Computational chemistry, through DFT calculations, shows that edge-type graphitic nitrogen is more effective towards ORR catalysis than pyridinic, pyrrolic, pyridonic, oxidized and basal-type graphitic nitrogen species.

Introduction

In an age dominated by an increasing worldwide demand for energy, the combustion of fossil fuels is still the main energy source which supports the requirements of the power system. However, the depletion of this energy system and the environmental concerns associated with its use, has led to huge scientific efforts on the use of renewable energy sources. Among these efforts, fuel cells (FCs) have been developed as a promising technology for energy supply and conversion as a substitute for combustion engines in vehicles[1]. In contrast to fossil fuels, these devices are not completely optimized, and they still present some limitations. One key factor in the development and commercialization of the FC is the oxygen reduction reaction (ORR) because of its slow kinetics and high overpotential[2,3]. In order to address this concern, the use of highly efficient electrocatalysts is necessary. The main disadvantage of the ORR catalysts is the use of platinum as electrocatalyst[4]. The low abundance in the Earth and the high price of this metal increases the total cost of the FC until values higher than current engines[2–4], which make these devices an unattractive alternative for widespread use.

One solution to overcome this problem is the design of low-cost electrocatalysts towards ORR. The work done on this topic can be classified into two groups according to the type of catalyst analysed or under development. The aim of the first of them is to replace platinum by another more abundant metal (usually a non-precious metal, such as Co[5] or Pd[6]) and, therefore, less expensive. The limitations of this strategy rely on the use of metals and the problems associated with them; that is, they have not reduced the cost significantly[7] and also metals can agglomerate or lixiviate, producing the loss of catalytic activity and a low durability[7]. The second and more innovative alternative is the development of metal-free catalysts based on heteroatom-doped carbon materials[8]. In this sense, nitrogen-doped carbon materials are one of the most promising materials due to their low price and high catalytic activity towards ORR. Moreover, N-doped

carbon materials are free from the carbon monoxide poisoning and they exhibit longer stability than platinum-based catalysts[8].

The study and development of advanced metal-free catalysts based on N-doped carbon materials have a large impact on the scientific community. The identification of the active sites towards ORR in these materials is mandatory for the design of advanced metal-free catalysts with platinum-like performance. However, there is a great controversy about the nature of active sites. On the basis of experimental results, some authors propose pyridinic N species[9–11] as responsible for the improvement in catalytic activity because of the conjugation effect of the nitrogen lone pair electrons and graphene π-system, which can increase the electron donor property and facilitate reductive O_2 adsorption. Nevertheless, there are studies that propose basal-type graphitic N (also referred to as quaternary N)[12,13] as the N functionality that reduces the electron density on the adjacent C atoms and facilitates the electron transfer from adjacent carbon atoms to N atoms and N back donation to adjacent C p_z orbitals. Moreover, experimental studies suggest that edge-type graphitic nitrogen[14,15] and pyrrolic nitrogen species[16,17] can also act as active sites. In recent years, N-C-O species[18,19] have also been proposed as active sites towards ORR due to the large positive charge density of the C atom adjacent to N and O atoms. This controversy of the experimental results is mainly due to the difficulty to isolate the nitrogen species in carbon materials while maintaining the morphology, structural order and electrical conductivity of the compared samples.

On the other hand, computer modelling studies have tried to overcome these limitations since studying isolated nitrogen species is easy in simulations[20]. However, the demonstration of the theoretical calculations has to be done through the comparison with experimental results. Therefore, the combination of both approaches is essential to understand the nature of the active sites in N-doped carbon materials.

In this context, this work presents an experimental method that permits the fine-tuning of N functionalities in N-doped carbon materials through a double stage heat treatment of polyaniline (PANI). The combination of a heat treatment in a slightly oxidant atmosphere followed by a

heat treatment in inert atmosphere, produces a selective etching of the carbon material that permits to tailor the N-species present in the material while maintaining the porosity and structural order. Therefore, the selective evaluation of the contribution in ORR from the different nitrogen species is possible. Furthermore, Density Functional Theory (DFT) calculations have been carried out in order to support the experimental results. Pyridinic, pyrrolic, basal and edge-type graphitic nitrogen, pyridonic and oxidized nitrogen functionalities have been computed towards oxygen reduction catalysis.

Experimental Section

Materials and reagents

Aniline was purchased from Sigma Aldrich and was distilled by refluxing under reduced pressure prior to its use in order to remove the impurities. Ammonium persulfate, ammonium hydroxide, potassium hydroxide (KOH) and Pt/Vulcan (20 wt% loading) were purchased from Sigma Aldrich. XC-72F Vulcan carbon black was supplied by Cabot Corporation. Hydrochloric acid (37% HCl) was purchased from VWR-Chemicals Prolabo. All the solutions were prepared using ultrapure water (18 MΩ cm from an Elga Labwater Purelab system). The gases N_2 (99.999%), O_2 (99.995%), H_2 (99.999%) and synthetic air were provided by Air Liquide and were used without any further purification or treatment.

PANI preparation

Polyaniline was prepared by chemical polymerization from a solution of 1 M HCl containing 0.067 M of aniline and ammonium persulfate in a stoichiometric ratio. The mixture was kept under stirring (500 rpm) for 3 h at 0 ºC. In order to remove the Cl^- counter ion, after the 2 h of the polymerization process, the obtained polymer was treated with 1 M NH_4OH for 24 h, resulting in PANI. The synthesized PANI was washed several times with distilled water and dried at 80 ºC overnight.

Heat treatment

150 mg of PANI was heat-treated in a tubular furnace by a two-step process. First, PANI was heat-treated under an oxygen-containing atmosphere (5000ppm O_2/N_2) at 1000 ºC for 1 h using a heating rate of 5 ºCmin^{-1} and, then, cooled down at room temperature at 10ºC·min^{-1}. The flow rate was maintained at 100 mLmin^{-1}. The sample obtained by this first treatment is named as PANI_O2_1000. The heat treatment under 5000 ppm of oxygen content in a nitrogen atmosphere at 1000ºC produces a carbon material with a higher yield and porosity than a heat treatment in nitrogen, as we already reported [18]. It seems that it favours crosslinking and condensation reactions that take place during the treatment, similar to a stabilization treatment of a softening material[18].

The second step consists of a heat treatment at 800, 1000 and 1200ºC for 1h using a heating rate of 5 ºCmin^{-1} under an inert (N_2) atmosphere. The flow rate was maintained at 200 mL·min^{-1}. The obtained samples are named as PANI_O2_1000_N2_X, being X the temperature of the second treatment, under inert (N_2) atmosphere. The furnaces were always purged for 1h before the heat treatment in the corresponding atmosphere and flow rate.

Physicochemical Characterization.

Raman spectra were collected on a Jasco NRS-5100 spectrometer. A 3.9 mW He-Ne laser at 633 nm was used. The spectra were acquired for 120 s. The detector was a Peltier cooled charge-coupled device (CCD) (1024 x 255 pixels). Calibration of the spectrometer was performed with a Si slice (521 ± cm^{-1}). The textural properties of the materials were evaluated by N_2 adsorption isotherms at -196 °C and CO_2 adsorption at 0ºC in an automatic adsorption system (Autosorb-6, Quantachrome). Prior to the measurements, the samples were degassed at 250 °C for 4 h. Apparent surface areas have been determined by BET method[21] (S_{BET}) and total micropore volume (pores of size < 2 nm) has been assessed by applying Dubinin-Radushkevich (DR) equation to the N_2 adsorption isotherms[22]. Temperature programmed desorption (TPD) experiments were performed in a DSC-TGA equipment (TA Instruments, SDT 2960 Simultaneous) coupled to a mass spectrometer (Thermostar, Balzers, GSD 300 T3) which was used to follow the m/z lines related to the decomposition of surface functional groups from the

surface of the carbon materials. The thermobalance was purged for 2 hours under a helium flow rate of 100 ml min^{-1} and then heated up to 950°C (heating rate 20°C min^{-1}). The surface composition and oxidation states of the elements of the prepared materials were studied using XPS in a VG-Microtech Mutilab 3000 spectrometer with an Al Kα radiation source (1253.6 eV). The deconvolution of the N1s XPS spectra was done by least squares fitting using Gaussian-Lorentzian curves, while a Shirley line was used for the background determination.

Electrocatalytic activity towards ORR

The study of the electrocatalytic activity towards ORR was performed in an Autolab PGSTAT302 (Metrohm, Netherlands) potentiostat. A rotating ring-disk electrode (RRDE, Pine Research Instruments, USA) equipped with a glassy carbon disk electrode (5.61 mm diameter) and an attached platinum ring was used as the working electrode, graphite as the counter electrode and a reversible hydrogen electrode (RHE) immersed in the working electrolyte through a Luggin as the reference electrode. The amount of catalyst on the disk electrode was optimized in order to reach the highest limiting current intensity, being 120 µg the optimum value. Therefore, the glassy carbon disk was modified with the samples using 120 µl of a 1 mg ml^{-1} dispersion of each carbon material (20% isopropanol, 0.02% Nafion®), obtaining a catalyst loading of 0.48 mg cm^{-2}. XC-72F Vulcan carbon black as a non-doped carbon material and 20wt%Pt/Vulcan samples were also used for comparison purposes. The electrocatalytic activity towards ORR was studied by linear sweep voltammetry (LSV) in O_2 saturated 0.1 M KOH solution between 1.0 and 0.0 V (vs. RHE) at different rotation rates, from 400 to 2025 rpm and at a scan rate of 5 mV s^{-1}. The potential of the ring electrode was held constant at 1.5 V (vs. RHE) during all measurements. The electron transfer number was calculated from the hydrogen peroxide oxidation in the Pt ring electrode as follows:

$$n = \frac{4\, I_d}{I_d + I_r/N}$$

Where I_r and I_d are the current measured at the ring electrode and the disk electrode, respectively, and N is the collection efficiency of the ring, which was experimentally

determined to be 0.37. Long-time stability test was also carried out for the most active sample in O_2-saturated 0.1 M KOH solution by cycling between 1.00 and 0.00 V vs RHE during 10,000 seconds at a scan rate of 5 $mV \cdot s^{-1}$.

Computer models

Density functional theory (DFT) at the B3LYP/6-31G(d) level was used in this study through Gaussian 09 software, using restricted and unrestricted Hamiltonians for closed shell (S=0) and open-shell (S=1/2) systems, respectively. Partial atomic charges were computed with Mülliken population analysis. The change in energies for each transformation was computed as the energy differences of optimized geometries neglecting vibrational corrections and are reported in eV (1 Hartree = 27.2116 eV). The model structures consist of a rectangular graphene carbon layer with 110 carbon atoms and 6x7 benzenic rings on zig-zag and armchair edges respectively. Since the properties of graphene flakes depend on size[23,24], the 6x7 rectangular flake was selected in order to represent more accurately graphene edges yet remaining computationally feasible. Self-consistent reaction field (SCRF) models of solvation, with the polarized continuum model (PCM)[25] representing the water medium were used in all models to account for the environment of the electrocatalytic experiment. The energy diagrams of ORR have been calculated based on the computational hydrogen electrode model potential, proposed by Norskov et. al[26]. The free energy change for each oxygen reduction stage is defined as $\Delta G = \Delta E' + \Delta G_{pH} + \Delta G_U$, where $\Delta E'$ is the difference of the DFT computed total energies, ΔG_{pH} and ΔG_U are the changes in free energies associated to the pH and electrode potential, respectively. $\Delta G_{pH} = k_B \cdot \ln 10 \cdot pH$, where k_B is Boltzmann´s constant and the pH is adjusted to 13, according to the 0.1 M KOH solution used during catalytic experimental results. $\Delta G_U = n \cdot e \cdot E$, where E is the electrode potential and n is the number of transferred electrons in each reduction step. The number of unpaired electrons has been considered in the models as follows; the pristine non-doped carbon and N-doped carbon configurations were computed as singlet, closed-shell states, for all cases. After the introduction of the electron-proton pairs, a doublet multiplicity was used

in the first and third reductions and to singlet state in the second and fourth reduction stages. The oxygen molecule ground state was computed as a triplet.

Results and discussion

Experimental results

Table 1 includes the heat treatment yields of the pre-treated and double stage treated samples. Fig. 1a shows the N_2-adsorption isotherms of PANI-derived carbon materials. All samples present type I isotherms, characteristic of microporous materials and the pore size distributions are similar in all the cases (Fig. 1b). The BET surface areas for the materials are similar, except for sample PANI_O2_1000_N2_800 which has a somewhat higher surface area. In this case, due to the preparation method, the oxygen groups created during the treatment (which includes cooling in the oxidative atmosphere) are removed when heating in N_2 at 800ºC resulting in some gasification and formation of porosity. However, the heat treatment at higher temperatures in N_2 (i.e., samples PANI_O2_1000_N2_1000 and PANI_O2_1000_N2_1200) produces, not only the oxygen groups removal but also some porosity shrinkage.

Table 1: Heat treatments yield, BET surface area, the atomic percentage of oxygen and nitrogen and atomic percentage of the nitrogen functionalities as determined from XPS.

Sample	Yield / %	BET surface area / $m^2 \cdot g^{-1}$	O content / at %	N content / at %	Pyridinic N content / at %	Pyridonic or pyrrolic N content / at %	Graphitic N content / at %	Oxidized N content / at %
PANI_O2_1000	36	1360	4.2	2.5	31	33	36	-
PANI_O2_1000_N2_800	33	1680	2.1	2.8	37	25	31	8
PANI_O2_1000_N2_1000	30	1440	2.7	2.3	30	18	47	5
PANI_O2_1000_N2_1200	27	1360	2.8	1.4	-	-	100	-

Concerning the structural order, Raman spectra for all samples are presented in Fig. 1c. The second treatment under inert atmosphere does not produce an important modification of the structural order since there is change neither in the D and G bands nor in the I_D/I_G ratio (I_D/I_G

close to 1.0 in all the samples). Therefore, all PANI-derived carbon materials are similar in pore size distribution and structural order.

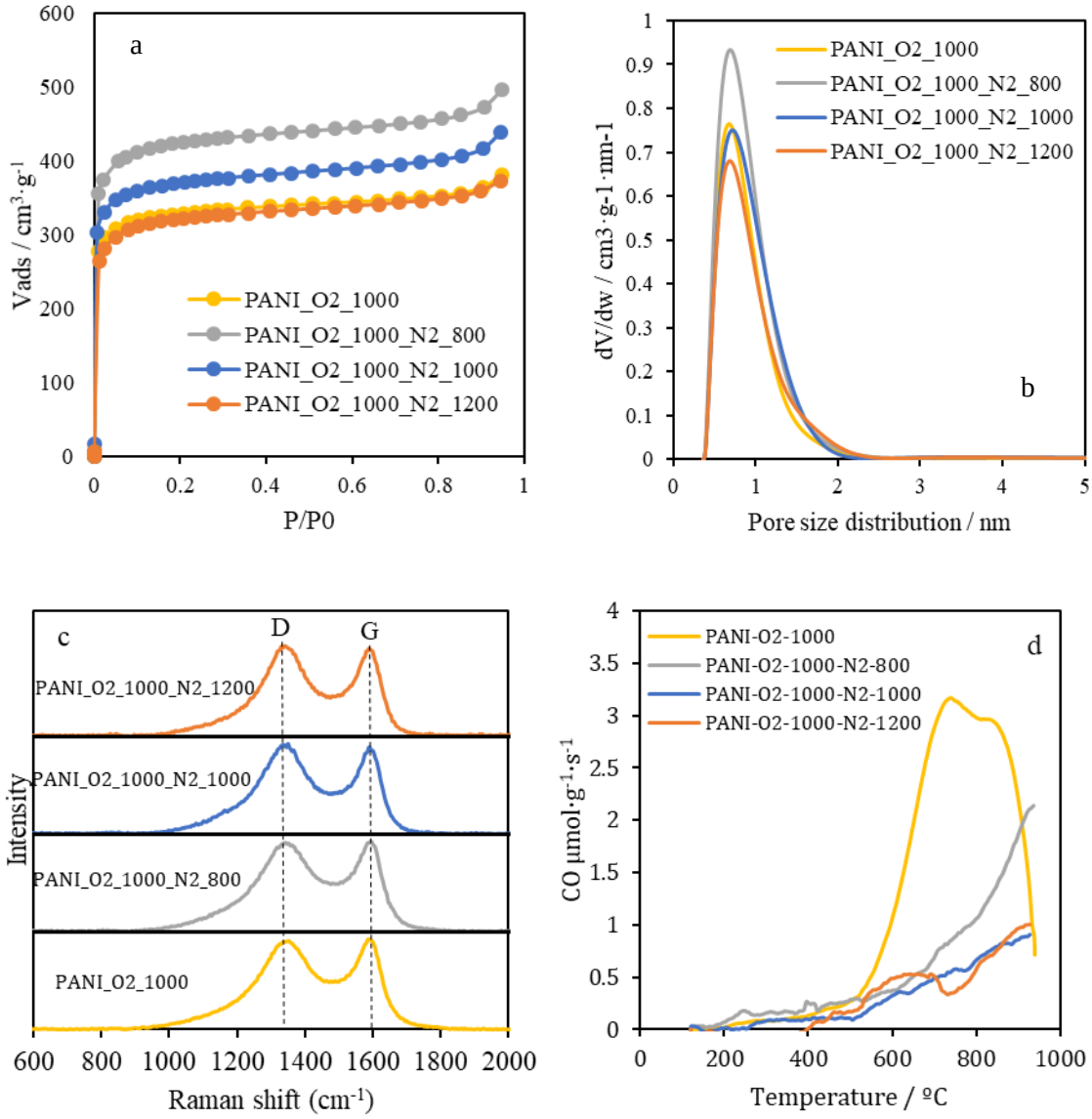

Fig. 1: (a) N_2-adsorption isotherms, (b) pore size distribution, (c) Raman spectra and (d) CO-TPD profiles of all materials.

The surface chemistry was studied by temperature-programmed desorption (TPD). The decomposition of surface oxygen functionalities using TPD is extensively used for characterizing the surface functionalities of carbon materials. CO_2 peaks results from carboxylic acids at temperatures below 500ºC and from lactones at temperature between 500-700ºC. Carboxylic anhydrides produces both CO and CO_2 peaks, while phenols and carbonyls produce both CO peaks at around 750 and 850ºC, respectively[27–30]. For these materials, CO_2 desorption

does not show relevant differences among all treatments. However, CO profiles reveal important changes. Fig. 1d shows the CO-TPD profiles for all PANI-derived carbon materials. N-doped carbon materials obtained by the pre-treatment under oxygen-containing atmosphere have a higher amount of oxygen groups because of the reaction between the oxygen from the atmosphere and the carbon materials[18]. This is especially remarkable in sample PANI_O2_1000 since the cooling is done in the oxygen-containing atmosphere. In this case, the CO-TPD profile exhibits a peak at around 750ºC, which is related to the presence of phenolic groups[18,29], and a second peak at around 850ºC that is associated with the presence of carbonyl/quinone groups[29]. For the rest of the samples, the higher the temperature of the second treatment in N_2 atmosphere, the lower the CO evolution. Therefore, the second treatment under inert atmosphere removes oxygen groups from the surface of the carbon materials. Interestingly, sample PANI_O2_1000_N2_1200 still shows some CO desorption in their TPD-profile, which can indicate that the carbon materials react with air once the heat treatment in inert atmosphere has finished and the sample is exposed to the environment, thereby creating oxygen groups.

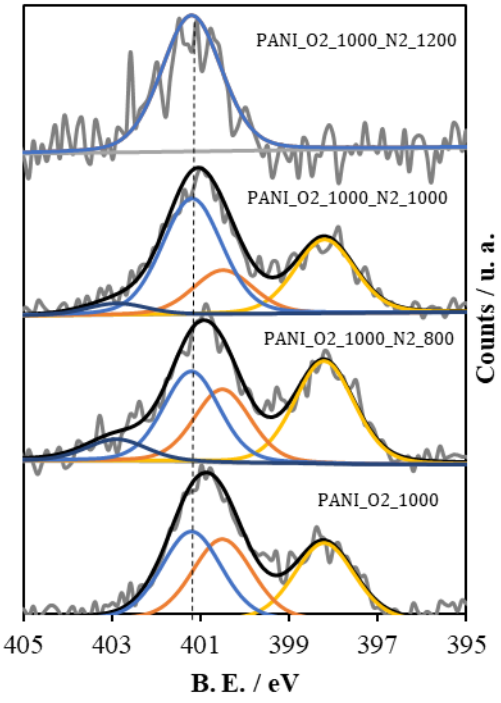

Fig. 2: N1s spectra of all PANI-derived carbon materials.

In order to identify the N functionalities in the PANI-derived carbon materials, XPS analyses have been performed. N1s spectra of all materials (Fig. 2) show differences in the type of nitrogen species present in the sample depending on the temperature of both treatments. The deconvolution of the N1s spectra has been done based on the literature[31–33]. All N-doped carbon materials mainly show three peaks; (i) pyridinic nitrogen at 398.2 eV, (ii) pyridonic and pyrrolic nitrogen at 400.5 eV and (iii) graphitic -type nitrogen species at 401.2 eV. In some samples, the presence of oxidized nitrogen is also observed at 402.9 eV (always below 10 at.%). The sample treated in the oxidizing atmosphere (sample PANI_O2_1000) has a high amount of pyridonic species (33 at.% in PANI_O2_1000), in agreement with our previous work[18]. Furthermore, the presence of pyridine and graphitic-type nitrogen species is also observed. Once the second treatment is applied in N_2 atmosphere at 800ºC, the pyridonic type species slightly decrease with an increase in the pyridinic type groups, what is in agreement with the loss of oxygen (see Table 1) and the CO-TPD profiles. Furthermore, if the second treatment is done at 1000ºC, an important decrease in the pyridinic and also pyridonic species is detected which occurs with the increase in the graphitic-type nitrogen species (Table 1). Interestingly, only one symmetric peak is detected in PANI_O2_1000_1200 at 401.2 eV. Complete disappearance of pyridinic and pyridonic species is observed and only graphitic-type nitrogen exists in this sample. This fact is strongly related to the already proposed transformation of pyridinic nitrogen (and also pyridonic species) into edge-type graphitic nitrogen atoms in zig-zag positions[14,32] from the condensation reactions that increase the size of the graphene layers[14,15,32]. Therefore, the presented experimental procedure seems to promote the formation of edge-type graphitic nitrogen in the carbon framework, maintaining the structural order and porosity.

The electrocatalytic activities towards ORR of all materials were studied in O_2-saturated 0.1M KOH solution (Fig. 3). Linear Sweep Voltammetry (LSV) analysis was performed using at RRDE at different rotation rates. The current registered in the Pt ring electrode is related to the amount of H_2O_2 formed in the disk electrode during the oxygen reduction reaction, which is the

intermediate compound found in the 2e- pathway. Fig. 3 shows the LSV curves and the number of transferred electrons at 1600 rpm for all samples in 0.1 M KOH electrolyte. The LSV for commercial 20 wt% Pt/Vulcan and a commercial non-doped carbon material (C) have been included for comparison purposes.

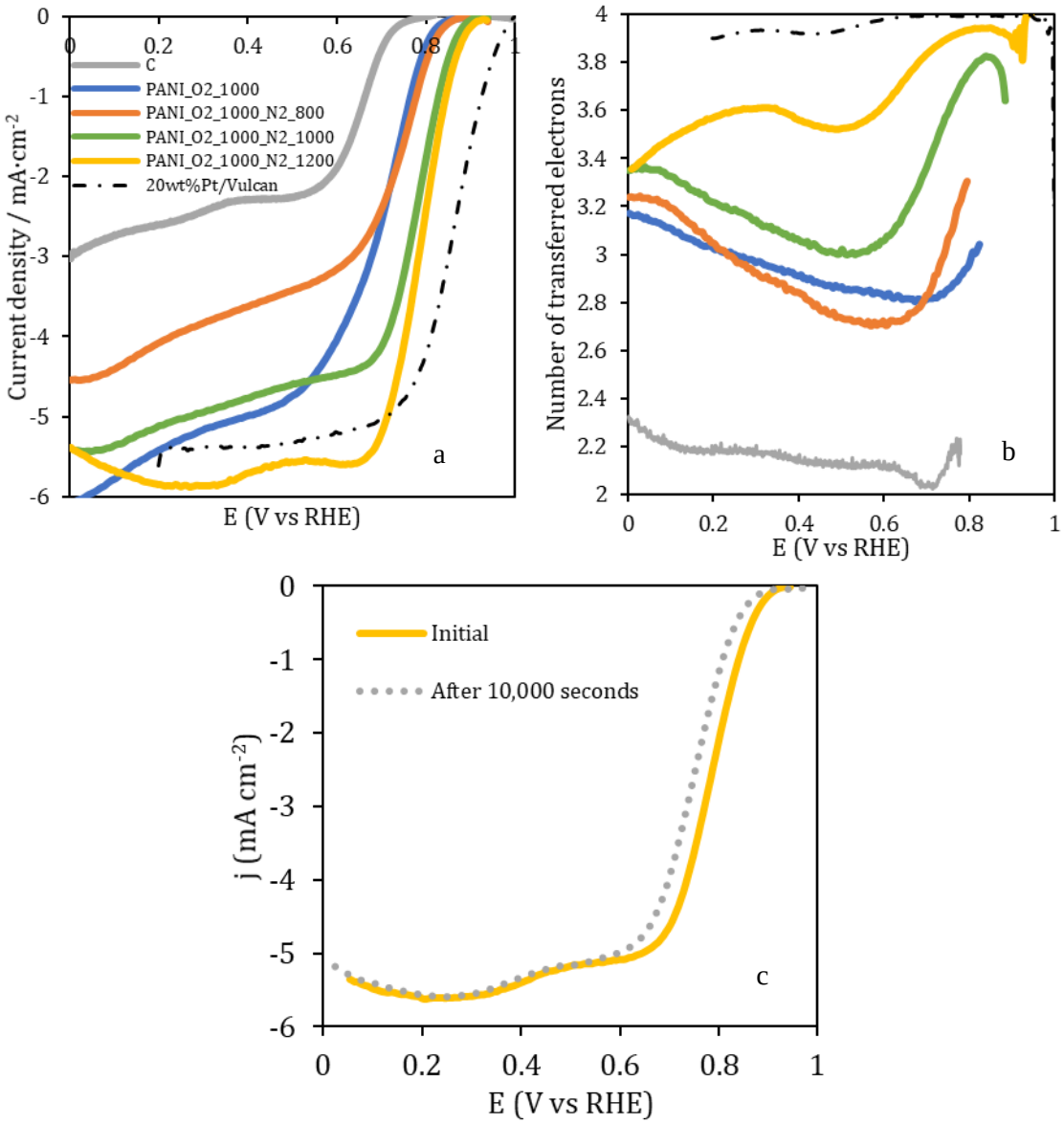

Fig. 3: (a) LSV curves and (b) the number of transferred electrons of PANI-derived carbon materials at 1600 rpm in an oxygen-saturated 0.1 M KOH solution, using a scan rate of 5 $mV \cdot s^{-1}$. (c) Long-time stability test of PANI_O2_1000_N2_1200 in an oxygen-saturated 0.1 M KOH solution at a scan rate of $5mV \cdot s^{-1}$.

The sample obtained by the oxygen-containing pre-treatment (PANI_O2_1000) has an interesting catalytic activity compared with the non-doped commercial carbon material (Fig. 3a). This enhancement can be mainly attributed to the pyridonic-type species formed by the

reaction between the molecular oxygen and nitrogen species of the PANI-derived carbon material during the heat treatment, as it has already been proposed[18].

Interestingly, significant differences are observed for samples obtained by the double stage heat treatment. The sample heat-treated under an inert atmosphere at 800ºC shows similar performance as the material obtained by treatment in the oxygen-containing atmosphere (PANI_O2_1000 sample) although with a lower limiting current (Fig. 3a). This seems to occur because this second treatment produces some decrease in pyridonic species with the corresponding increase in pyridines (see Table 1).

Interestingly, the higher the temperature used during such second treatment, the higher the catalytic activity of the carbon material. In fact, PANI-O2-1000-N2-1200 has the closest performance to the platinum catalyst mainly with respect to current density. According to XPS and TPD analysis, this high catalytic activity seems to be associated with the presence of graphitic nitrogen, since the transformation of pyridines and pyridones into edge-type graphitic species (See Table 1 and Fig. 2) results in an enhancement of the catalytic activity towards ORR. This fact is supported in the literature since edge-type graphitic nitrogen has been proposed as enhanced active centres for this reaction[14,15]. Graphitic N at edge sites cannot be clearly differentiated from internal, basal, locations with XPS. In contrast, the use of computational models allows us to explore directly both scenarios.

Fig. 3b displays the number of transferred electrons during the oxygen reduction reaction. The carbon materials prepared by one or two-stage heat treatments with a maximum temperature of 800ºC show a number of electrons close to 3, superior to the obtained by the non-doped carbon material. This means that the mechanism of the oxygen reduction reaction catalysed by these samples leads to hydrogen peroxide and water generation in the same percentage. Significant changes are observed when the second heat treatment temperature is 1000 ºC and, especially, 1200 ºC. In these samples, the number of transferred electrons increases significantly mainly at more positive potentials. This means that edge-type graphitic nitrogen species seem to favour

oxygen reduction through water generation. This behaviour was already observed in PANI-derived samples obtained by heat treatment at high temperatures[15].

Long-time stability test has also been carried out for the sample PANI_O2_1000_N2_1200 in 0.1 M KOH solution (Figure 3c). Interestingly, after 10,000 seconds of cycling the LSV profile of this sample shows almost identical limiting current density compared to the initial profile. The onset potential has shifted 0.02 V to more negative potentials. This probably could be related to the H_2O_2 generated at the low potential range, which can damage the most active species. A detailed study of this issue will be the subject of further research.

Computer modelling

DFT models were used to explore the role of the different potential sites of N-doped carbon materials towards oxygen reduction reaction. In this sense, all nitrogen functionalities found experimentally in N- doped carbon materials have been evaluated in the context of ORR. The effect of oxygen functional groups was not considered in the model as was not deemed fundamental in PANI-derived carbon materials. It has been argued that the oxidation of carbon materials increases the concentration of paramagnetic centres (via aryloxyl radical formation) and a high concentration of such centres promotes the decrease of hydrogen peroxide formation during ORR[34]. However, the oxygen reduction with oxidised pyrolytic graphite starts in the potential range of 0.6-0.8 V vs RHE[35]. Consequently, at potentials higher than 0.8 V, the oxygen reduction reaction would be mainly governed by nitrogen species and not by oxygen functional groups in PANI-derived carbon materials.

In addition, previous studies with carbon materials with different oxygen content (pristine material and heat treated) do not provide significant differences yielding similar catalytic activities[36]. In fact, the highest activity was observed when N species are introduced in the materials[36]. Experimentally, N functional groups favour the formation of sites with higher catalytic activity. Nevertheless, the combination of N and O species may be relevant if N-C-O

species are formed, which are also catalytic towards ORR[18]. Furthermore, the amount of O in PANI-derived carbon materials is low after the second heat treatment. Considering all this, oxygen groups were not considered in the models.

Fig. 4 shows relevant parts of the model structures used for all nitrogen functionalities. The full model structure consists of a carbon layer of 6 x 7 benzene rings where different functionalities have been introduced. The non-doped carbon material has also been included for comparison purposes.

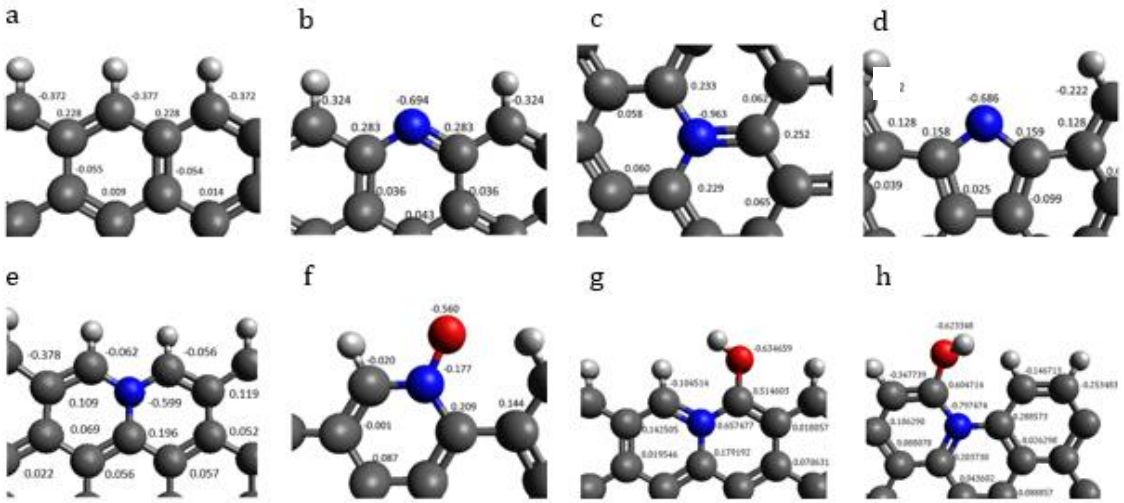

Fig. 4: Model structures and the atomic effective charge of: (a) non-doped carbon material, (b) pyridinic nitrogen, (c) basal-type graphitic nitrogen, (d) pyrrolic nitrogen, (e) edge-type graphitic nitrogen, (f) oxidized nitrogen, (g) pyridonic nitrogen in zig-zag position and (h) pyridonic nitrogen in armchair position. Hydrogen is white, carbon is grey nitrogen is blue, and oxygen is red.

In the alkaline aqueous environment, which are the conditions used in the experimental study, the ORR can be described by the following elementary steps[37]:

Four electrons pathway:

$$O_2 + \blacksquare \rightarrow O_2^{\blacksquare} \quad 1.1$$

$$O_2^{\blacksquare} + H_2O + e^- \rightarrow OOH^{\blacksquare} + OH^- \quad 1.2$$

$$OOH^{\blacksquare} + H_2O + e^- \rightarrow O^{\blacksquare} + OH^- + H_2O \quad 1.3$$

$$O^{\blacksquare} + H_2O + e^- \rightarrow OH^{\blacksquare} + OH^- \quad 1.4$$

$$OH^{\blacksquare} + H_2O + e^- \rightarrow H_2O + OH^- + \blacksquare \quad 1.5$$

$$O_2 + 2\,H_2O + 4\,e^- \rightarrow 4\,OH^-$$ Global

Two electrons pathway:

$$O_2 + \blacksquare \rightarrow O_2^{\blacksquare}$$ 2.1

$$O_2^{\blacksquare} + H_2O + e^- \rightarrow OOH^{\blacksquare} + OH^-$$ 2.2

$$OOH^{\blacksquare} + H_2O + e^- \rightarrow H_2O_2 + OH^- + \blacksquare$$ 2.3

$$O_2 + 2\,H_2O + 2\,e^- \rightarrow H_2O_2 + 2\,OH^-$$ Global

where ■ represents the catalytic active site for each N- or N- O- functional group and $X^{\blacksquare}$ represents the chemisorption of *X* species on the active site.

In order to illustrate the procedure used in the calculations, edge-type graphitic nitrogen species in a zig-zag edge position is chosen in the following discussion as an example. In all the cases, the computation has been done accordingly.

In the proposed mechanisms, the oxygen reduction reaction begins with the chemisorption of the oxygen molecule and there is some agreement on the identification of the catalytic active sites. The adjacent carbon atoms to the nitrogen suffer a change in their charge density, which can promote the oxygen chemisorption, being these considered as the active sites for the oxygen adsorption step[9,38]. Dissociative oxygen chemisorption has been proposed to occur through two carbon atoms[15,39] or a single carbon atom[40,41]. There are previous studies in which the dissociative O_2 chemisorption is proposed to occur on a single carbon active site, what makes necessary the presence of carbene type defects. This mechanism explains the catalytic activity of graphene (i.e., pure carbon materials)[40]. This approach is in agreement with previous studies in which it was demonstrated a correlation between ORR catalytic activity of non-doped carbon materials and the O_2 carbon gasification reactivity[42]. Thus, the presence of defects is necessary to explain the catalytic activity of pure carbon materials.

Recently, the catalytic activity of N-containing graphene has also been explained considering the presence of carbene species[41]. However, dissociative chemisorption can also be interpreted considering the chemisorption through two carbon atoms in a hydrogen terminated cluster[39,43]. In this study, all (both basal and edge-type) adjacent carbon atoms to the nitrogen are considered as possible active sites towards oxygen molecule chemisorption and all of them have been evaluated through terminal and bridging binding modes for the oxygen molecule. Hydrogen-terminated clusters have only been considered in this theoretical study which can be useful for comparison purposes.

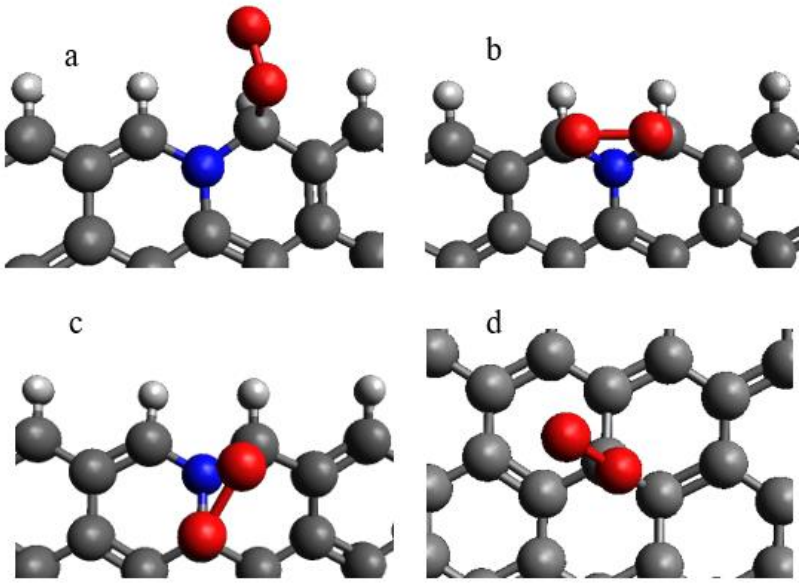

Fig. 5: Illustrative configurations for the oxygen chemisorption into edge-type graphitic nitrogen through: (a) one edge-carbon atom in a terminal binding mode, (b) two edge-carbon atoms in a bridging binding mode, (c) one basal-carbon atom and one edge-carbon atom in a bridging binding mode and (d) a non-doped basal position in a terminal binding mode. Hydrogen is white, carbon is grey, nitrogen is blue, and oxygen is red.

In the case of edge-type graphitic nitrogen used as an example, Fig. 5 illustrates possible oxygen chemisorption configurations where the adjacent carbon atoms play a role. Four possible conformations have been considered: the oxygen chemisorption through one active site in a terminal binding mode (Fig. 5a), two edge-carbon atoms in a bridging binding mode (Fig. 5b), a bridging binding mode through both one edge and one basal carbon atom (Fig. 5c) and the chemisorption in a basal carbon atom located at a distant position with respect to the N atom (Fig. 5d). Table 2 includes the chemisorption energies for all these conformations.

Table 2: Chemisorption energy of the different configurations in edge-type graphitic nitrogen.

Conformation (position/number of active sites)	**Chemisorption energy (eV)**
Edge / One (Fig. 5a)	0.07
Edge-Edge / Two (Fig. 5b)	-1.15
Basal-Edge / Two (Fig. 5c)	0.20
Basal / One (Fig. 5d)	No chemisorption occurs

The adsorption through a basal carbon atom located far from the N atom (Fig. 5d) is not favoured. In fact, the geometric optimization of the interaction between the chemisorption site and the oxygen molecule repels the oxygen molecule. This shows the difficulty for the basal chemical adsorption on pristine graphene. In addition, the adsorption through one active site (Fig. 5a) and through one basal-carbon atom and one edge-carbon atom in a bridging binding mode (Fig. 5c) are thermodynamically unfavored although with a low chemisorption energy. Only the adsorption configuration through two edge-carbon atoms in a bridging bonding mode (Fig. 5b) is thermodynamically favoured. This indicates that oxygen molecules react more easily with the edge carbon atoms adjacent to the nitrogen functionality, resulting in a C-O-O-C bridge binding as it was already proposed in literature[44].

Once the oxygen molecule is adsorbed in the most favourable chemisorption configuration, the next process is the first reduction or, in other words, the first electron and proton supply from the cathode and electrolyte (water in alkaline medium), respectively[26]. This is a common reaction in the 2 or 4 electron mechanisms.

In order to provide the correct intermediates, the reduction step has been managed as two consecutive processes. The reduction stage has been divided in first, the electron supply and, then, the proton supply. Applying this principle, interesting effects are observed in the DFT calculations. The electron addition to the chemisorbed intermediate through two active sites (C-

O-O-C bonds) shows that the charge on the oxygen atoms, approximately quantified as Mulliken charges, increases as a result of the electrons collection (Δδ(-) = 177%). Moreover, the distance of the oxygen-oxygen bond is slightly higher than that for the chemisorbed species without electron addition (from 1.41 A when the electron is not applied to 1.44 A), which evidences a weakening of the oxygen-oxygen bond. This behaviour can be taken as an early indication of the posterior rupture of the bond.

The oxygen-oxygen bond rupture of the chemisorbed species has been computed considering the addition of electrons during the reduction step. Fig. 6 illustrates this process comparing the effect of electrons supply. For the starting, positively charged, doped system, the cleavage of the oxygen-oxygen bond is unfavoured. Interestingly, this becomes favourable when one electron is supplied (-0.17 eV); and, if a second electron is added to the chemisorbed species, then the oxygen-oxygen bond rupture is heavily favoured (-1.13 eV). These results suggest that the electrons from the cathode are collected into the oxygen atoms, which weaken the oxygen-oxygen bond favouring its scission. This means that the reaction occurs through a dissociative mechanism for the oxygen molecule.

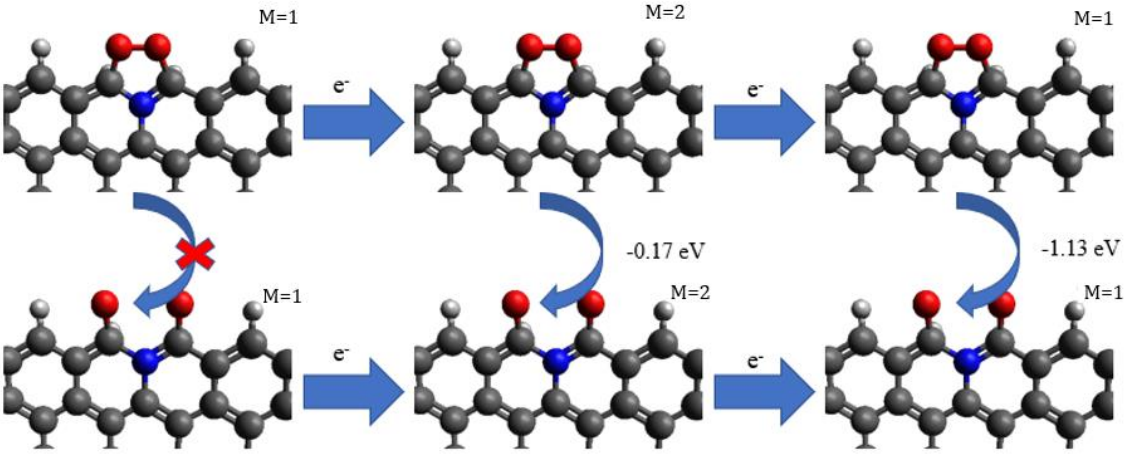

Fig. 6: Illustrative model of the geometries, multiplicity and energies during electron supply to the chemisorbed oxygen in a bridging binding mode through two edge-carbon atoms of the edge-type graphitic nitrogen species. Hydrogen is white, carbon is grey nitrogen is blue and oxygen is red.

After the electron supply, the proton must be introduced into the model structure to complete the first reduction stage. Fig. 7a illustrates this process. The proton is attracted towards the oxygen atoms that have collected the electrons forming an intramolecular hydrogen bond.

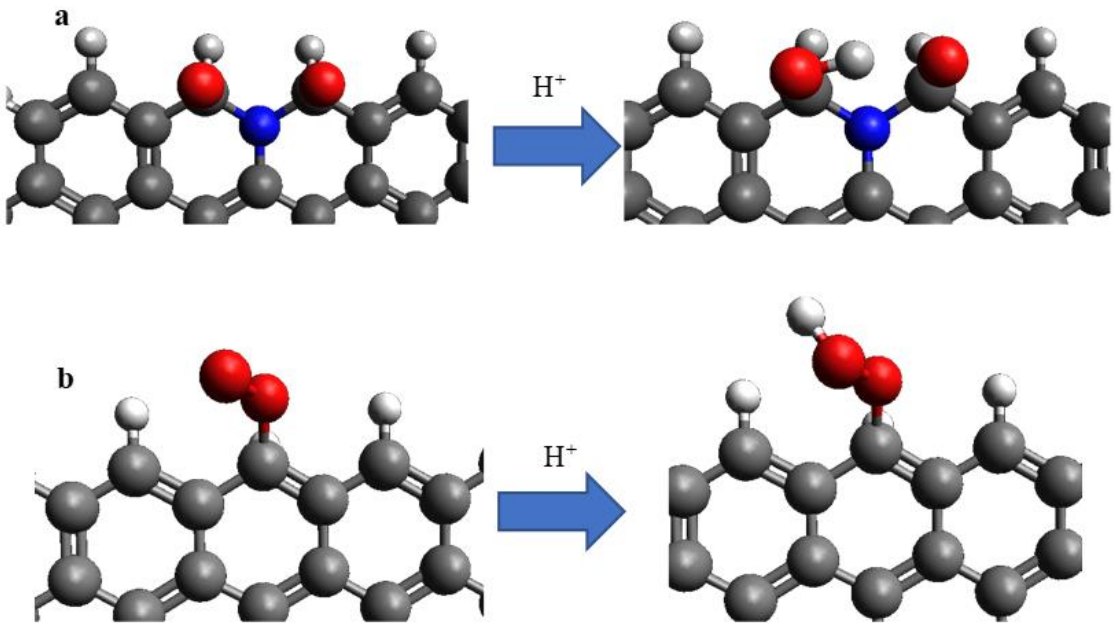

Fig. 7: Illustrative model of the configuration of the first electron-proton supply for N-doped (a) and non-doped materials (b). Hydrogen is white, carbon is grey, nitrogen is blue, and oxygen is red. Hydrogen is white, carbon is grey nitrogen is blue and oxygen is red.

In the case where the most thermodynamically favoured chemisorption is through a terminal binding mode, i.e., C-O-O bond, such as in the case of non-doped carbon materials, the first reduction stage leads to a C-O-O-H species[43] (Fig. 7b). This means that the oxygen chemisorption via two carbon active sites through a bridging binding mode, leads to a dissociative mechanism where the oxygen molecule is broken, whereas the chemical adsorption through one carbon active site (C-O-O) keeps bonded the oxygen molecule and the reduction occurs via an associative mechanism. However, if a carbene type defect is considered, then dissociative oxygen chemisorption may occur[40]. In N-doped carbon materials, it is commonly accepted that the oxygen reduction occurs via an associative mechanism[37], even for those works which focus on edge-type graphitic nitrogen[45]. Nevertheless, this is not the first time that a dissociative mechanism is proposed in edge-type graphitic nitrogen[38,43,44], which reinforces our hypothesis. The observation of the dissociative mechanism in edge-type graphitic nitrogen is possible when the electron supply and proton supply are separated into two steps, what makes reasonable to propose a modification in the reaction mechanism that fits better our experimental observations. It is also possible, that the presence of a carbene type defect in a neighbour carbon atom, favours the dissociative oxygen chemisorption through a single carbon atom[41].

The first oxygen reduction step for the other nitrogen functionalities has been computed following the same procedure as explained above. The next elementary steps for all the functionalities to achieve the final reduction of the oxygen molecule have also been calculated following the same methodology. This allows us to build the energy diagrams for the dioxygen reduction for all nitrogen species. Fig. 8 displays the computed energy diagrams for all nitrogen species. In addition, the diagram for the non-doped carbon material is also presented for comparison purposes.

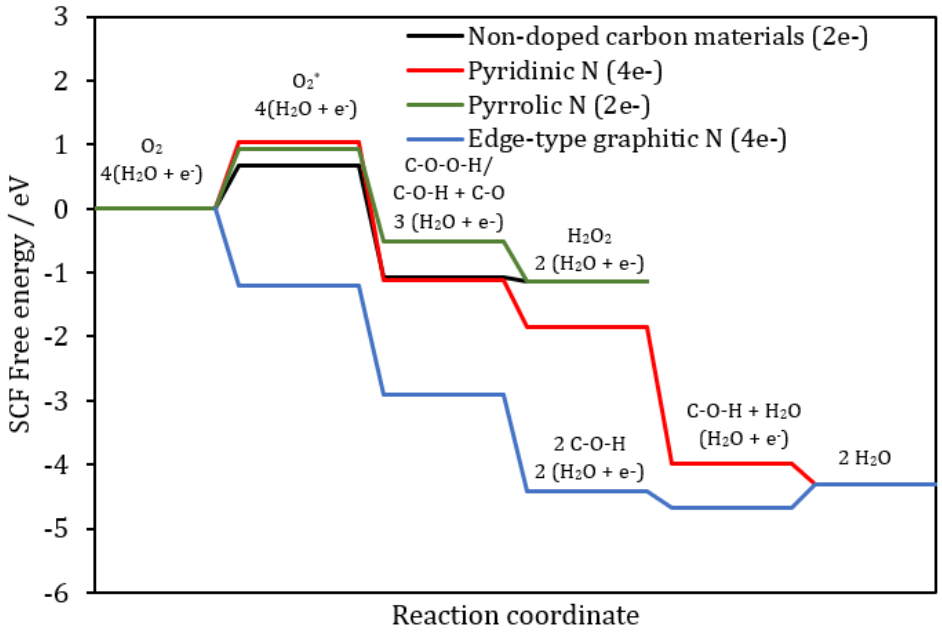

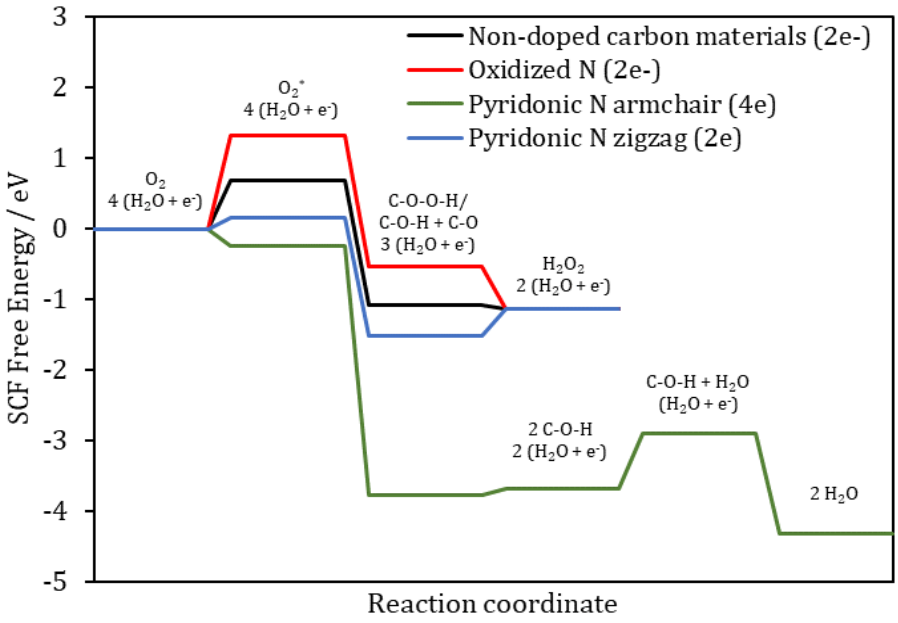

Fig. 8: SCF energy diagram for ORR of all nitrogen functionalities at 0.00 V.

Basal-type graphitic nitrogen is not presented in Fig. 8 because the oxygen molecule does not bond to the surface regardless of the staring geometry configuration (both for one and dual-site oxygen chemisorption), which reflects the poor catalytic activity of this site. Furthermore, pyridinic, pyrrolic and, especially, oxidized nitrogen functionalities show ORR stages with higher free energies than the non-doped carbon materials. The high energetic cost of the initial chemisorption step indicates that the presence of these species in carbon materials would not result in a relevant enhancement in their catalytic activity. The oxygen reduction reaction would mainly occur as in the non-doped carbon material.

Nevertheless, some nitrogen species significantly reduce the free energy of the ORR in carbon materials. The most favourable species for ORR is edge-type graphitic nitrogen functionalities, followed by pyridonic-type functionalities. Furthermore, the chemisorption of the oxygen molecule in a bridging binding mode (i.e., C-O-O-C bridge) through two adjacent carbon atoms of the edge-type graphitic nitrogen seems to favour the oxygen molecule dissociation, resulting in a four-electron mechanism forming two molecules of water at the end of the reduction.

Fig. 9 shows the SCF energy diagrams of edge-type graphitic nitrogen at different potentials. The diagram for E = 0.000 V corresponds to the reaction running by short-circuiting the cell,

where all elementary steps are strongly exothermic. However, by shifting the potential to the thermodynamic potential (1.229 V), the second, third and fourth reduction processes become uphill, being the last one the step that shows the higher free energy (1.44 eV) and, therefore, it could be the rate-limiting step. This reinforces the need for applying an overpotential to solve the limiting barriers and get an adequate reaction rate.

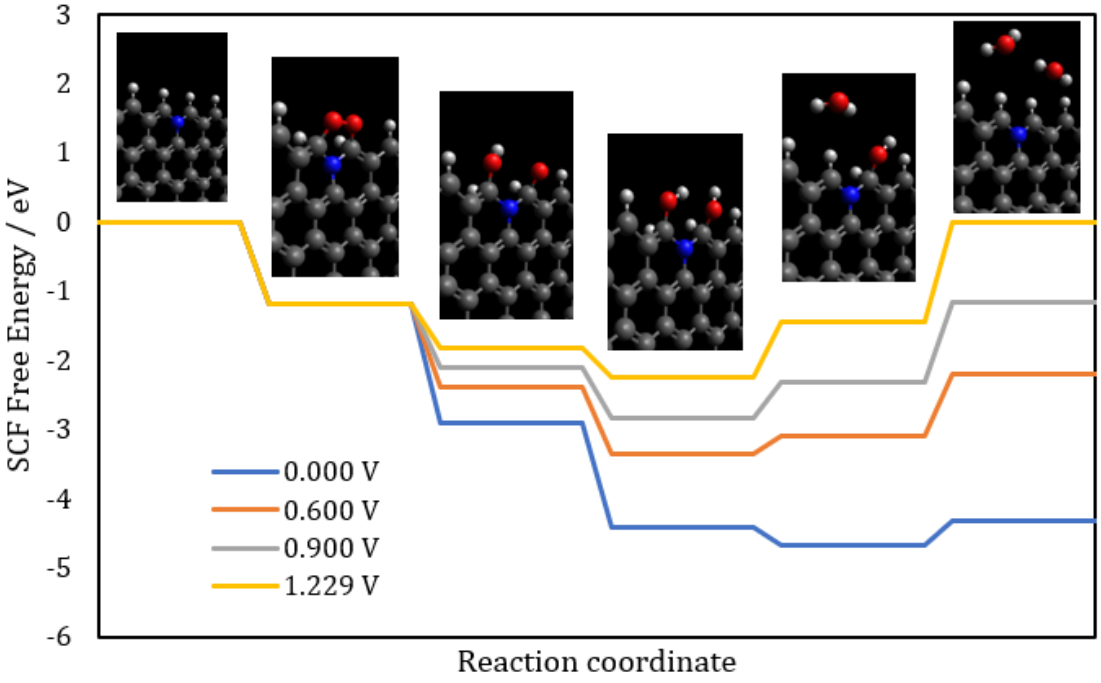

Fig. 9: SCF energy diagram for ORR of edge-type graphitic nitrogen at 1.229 and 0.000 V. Hydrogen is white, carbon is grey, nitrogen is blue, and oxygen is red.

On the basis of the catalytic test for PANI_O2_1000_N2_1200 (Fig. 3), other relevant potentials have been computed. At 0.900 V (approximately the onset potential measured for this sample, Fig. 3), the second and third reduction step becomes more thermodynamically favourable and, moreover, a slightly energetic decrease in the fourth oxygen reduction stage is observed (1.15 eV). These results may be used to indicate the beginning of the ORR. Furthermore, at 0.600 V (where approximately the limiting current density is achieved, Fig. 3), the free energy is much lower (0.73 eV), what could be an indicator of efficient catalysis.

The results of this computational study are fully consistent with the catalytic activities of PANI-derived carbon materials. The experimental results show that the transformation of pyridinic and pyridonic nitrogen species into edge-type graphitic nitrogen species is responsible for the highly

efficient electrocatalysis with high water selectivity. The sample containing mainly graphitic N species (i.e., sample PANI_O2_1000_N2_1200) is the one having the highest activity and selectivity towards the 4 electrons mechanism. Moreover, the chemisorption of the oxygen molecule in a bridging binding mode, which leads to a dissociative mechanism, can explain why the oxygen reduction reaction for the materials containing these species occurs through four electrons pathway. Nevertheless, other active sites like defects[40,41] are possible and may contribute to the ORR in these complex systems.

The sample only treated in an oxygen-containing atmosphere (that is, without applying the second heat treatment in N_2, PANI_O2_1000) shows a better performance towards ORR than a non-doped carbon material, although it is inferior to the double heat treatment PANI-derived carbon materials. This can be due to the presence of pyridonic-type species, as deduced from TPD and XPS analysis. The computational results are consistent with the experimental results (Fig. 8). The N-C-O species can catalyse the ORR in an easier way than for non-doped carbon materials, but their catalysis is poorer than the obtained by edge-type graphitic nitrogen species. Furthermore, DFT calculations also show differences between the armchair and zig-zag positions for pyridonic species. Whereas the armchair position seems to favour the reduction via 4 electrons pathway, the zig-zag position leads to oxygen molecule chemisorption through one edge-carbon atom in a terminal binding mode configuration, resulting in a 2 electrons reduction process. However, both functionalities show similar limiting energetic barriers what can explain why the sample prepared by treatment only in the oxygen-containing atmosphere has a number of transferred electrons close to 3, suggesting that the population of both functionalities can be similar.

Conclusions

N-doped carbon materials have been prepared through a double stage heat treatment of polyaniline, first under an oxygen-containing atmosphere at 1000ºC and, then, under inert atmosphere in a range of temperatures between 800 and 1200ºC. PANI-derived carbon materials were characterized by Raman spectroscopy, XPS, TPD and N_2-adsorption isotherms. The

detailed characterization demonstrates that the samples pre-treated only with the oxygen-containing atmosphere have a higher amount of surface oxygen groups, and the N-species are mainly pyridonic groups. Once the second treatment is applied, the high-temperature treatment using inert atmosphere promotes the transformation of pyridinic nitrogen to graphitic nitrogen species, resulting in a material which essentially contains only this species. All these changes in the chemical nature of the functional groups are not accompanied by important modifications in porosity and structural order. The resultant carbon materials exhibit near platinum-like performance towards ORR with high selectivity towards water generation. DFT calculations were carried out considering all nitrogen functionalities and the results are contrasted with the experiments. The computational results are in excellent agreement with the experimental results, reinforcing the key role that edge-type graphitic nitrogen plays as the most active and selective catalytic site for ORR.

Conflict of Interest

The authors declare no conflict of interest.

Acknowledgements

The authors thank Ministerio de Ciencia, Innovación y Universidades and FEDER for financial support (Project RTI2018-095291-B-I00, ENE2017-90932-REDT and FIS2015-64222-C2-2-P).

References

1 B. C. Steele and A. Heinzel, *Nature*, 2001, **414**, 345–352.

2 Y. Nie, L. Li and Z. Wei, *Chem. Soc. Rev.*, 2015, **44**, 2168–2201.

3 I. E. L. Stephens, A. S. Bondarenko, U. Grønbjerg, J. Rossmeisl and I. Chorkendorff, *Energy Environ. Sci.*, 2012, **5**, 6744.

4 Y. Jiao, Y. Zheng, M. Jaroniec and S. Z. Qiao, *Chem. Soc. Rev.*, 2015, **44**, 2060–2086.

5 A. Gabe, J. García-Aguilar, Á. Berenguer-Murcia, E. Morallón and D. Cazorla-Amorós, *Appl. Catal. B Environ.*, 2017, **217**, 303–312.

6 J. Zhang, M. B. Vukmirovic, Y. Xu, M. Mavrikakis and R. R. Adzic, *Angew. Chemie - Int. Ed.*, 2005, **44**, 2132–2135.

7 F. Jaouen, E. Proietti, M. Lefèvre, R. Chenitz, J.-P. Dodelet, G. Wu, H. T. Chung, C. M. Johnston and P. Zelenay, *Energy Environ. Sci.*, 2011, **4**, 114–130.

8 L. Dai, Y. Xue, L. Qu, H.-J. Choi and J.-B. Baek, *Chem. Rev.*, 2015, **115**, 4823–4892.

9 D. Guo, R. Shibuya, C. Akiba, S. Saji, T. Kondo and J. Nakamura, *Science*, 2016, **351**, 361–365.

10 C. V. Rao, C. R. Cabrera and Y. Ishikawa, *J. Phys. Chem. Lett.*, 2010, **1**, 2622–2627.

11 T. Xing, Y. Zheng, L. H. Li, B. C. C. Cowie, D. Gunzelmann, S. Z. Qiao, S. Huang and Y. Chen, *ACS Nano*, 2014, **8**, 6856–6862.

12 K. Gong, F. Du, Z. Xia, M. Durstock and L. Dai, *Science*, 2009, **323**, 760–764.

13 L. Lai, J. R. Potts, D. Zhan, L. Wang, C. K. Poh, C. Tang, H. Gong, Z. Shen, J. Lin and R. S. Ruoff, *Energy Environ. Sci.*, 2012, **5**, 7936.

14 T. Sharifi, G. Hu, X. Jia and T. Wågberg, *ACS Nano*, 2012, **6**, 8904–8912.

15 J. Quílez-Bermejo, E. Morallón and Cazorla-Amorós, *Chem. Commun*, ***54***, *4441-4444.*

16 W. Ding, Z. Wei, S. Chen, X. Qi, T. Yang, J. Hu, D. Wang, L. J. Wan, S. F. Alvi and L. Li, *Angew. Chemie - Int. Ed.*, 2013, **52**, 11755–11759.

17 J. Zheng, C. Guo, C. Chen, M. Fan, J. Gong, Y. Zhang, T. Zhao, Y. Sun, X. Xu, M. Li, R. Wang, Z. Luo and C. Chen, *Electrochim. Acta*, 2015, **168**, 386–393.

18 J. Quílez-Bermejo, C. González-Gaitán, E. Morallón and D. Cazorla-Amorós, *Carbon*, 2017, **119**, 62–71.

19 R. Silva, D. Voiry, M. Chhowalla and T. Asefa, *J. Am. Chem. Soc.*, 2013, **135**, 7823–7826.

20 L. Zhang, C. Y. Lin, D. Zhang, L. Gong, Y. Zhu, Z. Zhao, Q. Xu, H. Li and Z. Xia, *Adv. Mater.*, 2018, **1805252**, 1–16.

21 S. Brunauer, P. H. Emmett and E. Teller, *J. Am. Chem. Soc.*, 1938, **60**, 309–319.

22 M. M. Dubinin, *Chem. Rev.*, 1960, **60**, 235–241.

23 K. Nakada, M. Fujita, G. Dresselhaus and M. S. Dresselhaus, 1996, **54**, 17954–17961.

24 S. E. Stein and R. L. Brown, *J. Am. Chem. Soc.*, 1987, **109**, 3721–3729.

25 J. Tomasi, B. Mennucci and R. Cammi, *Chem. Rev.*, 2005, **105**, 2999–3094.

26 J. K. Nørskov, J. Rossmeisl, A. Logadottir, L. Lindqvist, J. R. Kitchin, T. Bligaard and H. Jónsson, *J. Phys. Chem. B*, 2004, **108**, 17886–17892.

27 H. F. Gorgulho, J. P. Mesquita, F. Gonçalves, M. F. R. Pereira and J. L. Figueiredo, *Carbon*, 2008, **46**, 1544–1555.

28 R. Berenguer, J. P. Marco-Lozar, C. Quijada, D. Cazorla-Amorós and E. Morallón, *Carbon*, 2009, **47**, 1018–1027.

29 J. Figueiredo, M. F. Pereira, M. M. Freitas and J. J. Órfão, *Carbon*, 1999, **37**, 1379–1389.

30 Y. Otake and R. G. Jenkins, *Carbon*, 1993, **31**, 109–121.

31 E. Raymundo-Piñero, D. Cazorla-Amorós and Á. Linares-Solano, *Carbon*, 2003, **41**, 1925–1932.

32 J. R. Pels, F. Kapteijn, J. A. Moulijn, Q. Zhu and K. M. Thomas, *Carbon*, 1995, **33**, 1641–1653.

33 M. Jaymand, *Prog. Polym. Sci.*, 2013, **38**, 1287–1306.

34 J. Balej, K. Balogh, P. Stopka and O. Špalek, *Collect. Czechoslov. Chem. Commun.*, 1980, **45**, 3249–3253.

35 C. Paliteiro, A. Hamnett and J. B. Goodenough, *J. Electroanal. Chem.*, 1987, **233**, 147–159.

36 M. J. Mostazo-López, D. Salinas-Torres, R. Ruiz-Rosas, E. Morallón and D. Cazorla-Amorós, *Materials*, 2019, **12**, 1–17.

37 K. H. Wu, D. W. Wang, D. S. Su and I. R. Gentle, *ChemSusChem*, 2015, **8**, 2772–2788.

38 G. L. Chai, Z. Hou, D. J. Shu, T. Ikeda and K. Terakura, *J. Am. Chem. Soc.*, 2014, **136**, 13629–13640.

39 T. Ikeda, M. Boero, S. F. Huang, K. Terakura, M. Oshima and J. Ozaki, *J. Phys. Chem. C*, 2008, **112**, 14706–14709.

40 L. R. Radovic, *J. Am. Chem. Soc.*, 2009, **131**, 17166–17175.

41 L. R. Radovic, in the World Conference of *Carbon*, Lexington, Kentucky, 2019.

42 A. Gabe, R. Ruiz-Rosas, E. Morallón and D. Cazorla-Amorós, *Carbon*, 2019, **148**, 430–440.

43 T. Ikeda, Z. Hou, G. L. Chai and K. Terakura, *J. Phys. Chem. C*, 2014, **118**, 17616–17625.

44 X. Hou, Q. Hu, P. Zhang and J. Mi, *Chem. Phys. Lett.*, 2016, **663**, 123–127.

45 D. P. Wilkinson, Z.-S. Liu, Z. Shi, H. Wang and J. Zhang, *Electrochim. Acta*, 2005, **51**, 1905–1916.